

Depth-resolved model-based reconstruction of attenuation coefficients in optical coherence tomography

K. A. Vermeer,^{1,*} J. Mo,² J. J. A. Weda,² H. G. Lemij,³
and J. F. de Boer^{1,2,4}

¹Rotterdam Ophthalmic Institute, Rotterdam Eye Hospital,
P.O. Box 70030, 3000 LM Rotterdam, The Netherlands

²LaserLaB Amsterdam, VU University

De Boelelaan 1081, 1081 HV Amsterdam, The Netherlands

³Glaucoma Service, Rotterdam Eye Hospital,

P.O. Box 70030, 3000 LM Rotterdam, The Netherlands

⁴Dept. of Physics and Astronomy, VU University

De Boelelaan 1081, 1081 HV Amsterdam, The Netherlands

*k.vermeer@eyehospital.nl

Abstract: We present a method, based on a single scattering model, to calculate the attenuation coefficient of each pixel in optical coherence tomography (OCT) depth profiles. Numerical simulations were used to determine the model's response to different depths and attenuation coefficients. Experiments were performed on uniform and layered phantoms with varying attenuation coefficients. They were measured by a 1300 nm OCT system and their attenuation coefficients were evaluated by our proposed method and by fitting the OCT slope as the gold standard. Both methods showed largely consistent results for the uniform phantoms. On the layered phantom, only our proposed method accurately estimated the attenuation coefficients. For all phantoms, the proposed method largely reduced the variability of the estimated attenuation coefficients. The method was illustrated on an in-vivo retinal OCT scan, effectively removing common imaging artifacts such as shadowing. By providing localized, per-pixel attenuation coefficients, this method enables tissue characterization based on attenuation coefficient estimates from OCT data.

© 2013 Optical Society of America

OCIS codes: (110.3010) Image reconstruction techniques; (110.3200) Inverse scattering; (110.4500) Optical Coherence Tomography; (170.4500) Optical coherence tomography; (170.4580) Optical diagnostics for medicine; (170.6935) Tissue characterization

References and links

1. R. Kuc, "Clinical application of an ultrasound attenuation coefficient estimation technique for liver pathology characterization," *IEEE Trans. Biomed. Eng.* **27**, 312–319 (1980).
2. G. Berger, P. Laugier, J. C. Thalabard, and J. Perrin, "Global breast attenuation: Control group and benign breast diseases," *Ultrasonic Imaging* **12**, 47–57 (1990).
3. K. B. Sagar, D. H. Agemura, W. D. O'Brien, L. R. Pelc, T. L. Rhyne, L. S. Wann, R. A. Komorowski, and D. C. Warltier, "Quantitative ultrasonic assessment of normal and ischaemic myocardium with an acoustic microscope: relationship to integrated backscatter," *Cardiovasc. Res.* **24**, 447–455 (1990).
4. Y. Sugata, K. Murakami, M. Ito, T. Shiina, and Y. Yamamoto, "An application of ultrasonic tissue characterization to the diagnosis of cataract," *Acta Ophthalmologica* **70**, 35–39 (1992).

5. F. J. van der Meer, D. J. Faber, D. M. B. Sassoon, M. C. Aalders, G. Pasterkamp, and T. G. van Leeuwen, "Localized measurement of optical attenuation coefficients of atherosclerotic plaque constituents by quantitative optical coherence tomography," *IEEE Trans. Med. Imaging* **24**, 1369–1376 (2005).
6. C. Xu, J. M. Schmitt, S. G. Carlier, and R. Virmani, "Characterization of atherosclerosis plaques by measuring both backscattering and attenuation coefficients in optical coherence tomography," *J. Biomed. Opt.* **13**, 034003 (2008).
7. G. van Soest, T. Goderie, E. Regar, S. Koljenović, G. L. J. H. van Leenders, N. Gonzalo, S. van Noorden, T. Okamura, B. E. Bouma, G. J. Tearney, J. W. Oosterhuis, P. W. Serruys, and A. F. W. van der Steen, "Atherosclerotic tissue characterization in vivo by optical coherence tomography attenuation imaging," *J. Biomed. Opt.* **15**, 011105 (2010).
8. R. A. McLaughlin, L. Scolaro, P. Robbins, C. Saunders, S. L. Jacques, and D. D. Sampson, "Parametric imaging of cancer with optical coherence tomography," *J. Biomed. Opt.* **15**, 046029 (2010).
9. K. Barwari, D. M. de Bruin, E. C. Cauberg, D. J. Faber, T. G. van Leeuwen, H. Wijkstra, J. de la Rosette, and M. P. Laguna, "Advanced diagnostics in renal mass using optical coherence tomography: a preliminary report," *J. Endourol.* **25**, 311–3115 (2011).
10. K. Barwari, D. M. de Bruin, D. J. Faber, T. G. van Leeuwen, J. J. de la Rosette, and M. P. Laguna, "Differentiation between normal renal tissue and renal tumours using functional optical coherence tomography: a phase I in vivo human study," *BJU International* **110**, E415–E420 (2012).
11. P. H. Tomlins, O. Adegun, E. Hagi-Pavli, K. Piper, D. Bader, and F. Fortune, "Scattering attenuation microscopy of oral epithelial dysplasia," *J. Biomed. Opt.* **15**, 066003 (2010).
12. Q. Q. Zhang, X. J. Wu, T. Tang, S. W. Zhu, Q. Yao, B. Z. Gao, and X. C. Yuan, "Quantitative analysis of rectal cancer by spectral domain optical coherence tomography," *Phys. Med. Biol.* **57**, 10 (2012).
13. J. van der Schoot, K. A. Vermeer, J. F. de Boer, and H. G. Lemij, "The effect of glaucoma on the optical attenuation coefficient of the retinal nerve fiber layer in spectral domain optical coherence tomography images," *Invest Ophthalmol Vis Sci* **53**, 2424–2430 (2012).
14. K. A. Vermeer, J. van der Schoot, H. G. Lemij, and J. F. de Boer, "RPE-normalized RNFL attenuation coefficient maps derived from volumetric OCT imaging for glaucoma assessment," *Invest Ophthalmol Vis Sci* **53**, 6102–6108 (2012).
15. F. J. van der Meer, D. J. Faber, M. C. Aalders, J. Perree, and T. G. J. M. van Leeuwen, "Detection of apoptosis by optical coherence tomography (OCT)," *Proc. SPIE* **4251**, 165–169 (2001).
16. F. van der Meer, D. Faber, M. Aalders, A. Poot, I. Vermes, and T. van Leeuwen, "Apoptosis- and necrosis-induced changes in light attenuation measured by optical coherence tomography," *Lasers Med. Sci.* **25**, 259–267 (2010).
17. J. Li, C. Chen, B. Chen, Z. Shen, Y. He, Y. Xia, and S. Liu, "Quantitative discrimination of NPC cell lines using optical coherence tomography," *J. Biophoton.* **5**, 544–549 (2012).
18. J. Li, Z. Tu, Z. Shen, Y. Xia, Y. He, S. Liu, and C. Chen, "Quantitative measurement of optical attenuation coefficients of cell lines CNE1, CNE2, and NP69 using optical coherence tomography," *Lasers Med. Sci.* **28**, 621–625 (2013).
19. K. A. Vermeer, J. van der Schoot, H. G. Lemij, and J. F. de Boer, "Quantitative RNFL attenuation coefficient measurements by RPE-normalized OCT data," *Proc. SPIE* **8209**, 8209U (2012).
20. K. A. Vermeer, J. van der Schoot, H. G. Lemij, and J. F. de Boer, "Automated segmentation by pixel classification of retinal layers in ophthalmic OCT images," *Biomed. Opt. Express* **2**, 1743–1756 (2011).
21. J. M. Schmitt, A. Knuttel, M. Yablowsky, and M. A. Eckhaus, "Optical-coherence tomography of a dense tissue - statistics of attenuation and backscattering," *Phys. Med. Biol.* **39**, 1705–1720 (1994).
22. D. J. Faber, F. J. van der Meer, M. C. G. Aalders, and T. G. van Leeuwen, "Quantitative measurement of attenuation coefficients of weakly scattering media using optical coherence tomography," *Opt. Express* **12**, 4353–4365 (2004).
23. T. G. van Leeuwen, D. J. Faber, and M. C. Aalders, "Measurement of the axial point spread function in scattering media using single-mode fiber-based optical coherence tomography," *IEEE J. Sel. Top. Quantum Electron.* **9**, 227–233 (2003).
24. D. I. Hughes and F. A. Duck, "Automatic attenuation compensation for ultrasonic imaging," *Ultrasound Med. Biol.* **23**, 651–664 (1997).
25. D. M. de Bruin, R. H. Bremmer, V. M. Kodach, R. de Kinkelder, J. van Marle, T. G. van Leeuwen, and D. J. Faber, "Optical phantoms of varying geometry based on thin building blocks with controlled optical properties," *J. Biomed. Opt.* **15**, 025001 (2010).
26. J. A. Li, M. de Groot, F. Helderma, J. H. Mo, J. M. A. Daniels, K. Grunberg, T. G. Sutedja, and J. F. de Boer, "High speed miniature motorized endoscopic probe for optical frequency domain imaging," *Opt. Express* **20**, 24132–24138 (2012).
27. M. J. A. Girard, N. G. Strouthidis, C. R. Ethier, and J. M. Mari, "Shadow removal and contrast enhancement in optical coherence tomography images of the human optic nerve head," *Invest Ophthalmol Vis Sci* **52**, 7738–7748 (2011).
28. P. Lee, W. Gao, and X. Zhang, "Performance of single-scattering model versus multiple-scattering model in the determination of optical properties of biological tissue with optical coherence tomography," *Appl. Opt.* **49**,

1. Introduction

The power of a coherent light beam propagating through a turbid medium is attenuated along its path due to scattering and absorption. The attenuation depends on the specific optical properties of that medium and is governed by its attenuation coefficient. The irradiance (power per unit area) of the coherent light beam that propagates through a (homogeneous) medium is given by Lambert-Beer's law

$$L(z) = L_0 e^{-\mu z}, \quad (1)$$

where $L(z)$ is the irradiance of the beam after traveling through the medium over a distance z , L_0 is the irradiance of the incident light beam and μ is the attenuation coefficient. Large attenuation coefficients result in a quick and exponential decline of the irradiance of the coherent light beam with depth. Because the attenuation coefficient is an optical property of the medium, determining the attenuation coefficient provides valuable information on the composition of this medium.

In biomedical applications, the attenuation coefficient has been used for various diagnostic or classification purposes over the last decades. The acoustic attenuation coefficient was first applied in ultrasound for a range of applications such as liver pathology characterization [1], breast diseases [2], myocardial ischaemia [3] and cataract [4]. Later, attenuation coefficients were measured by optical methods, including optical coherence tomography (OCT), for application such as atherosclerotic plaque characterization [5–7], cancer in axillary lymph node [8], renal tumor tissue [9, 10], oral cancer [11], rectal cancer [12] and glaucoma diagnosis and monitoring [13, 14]. Attenuation coefficients were also found to correlate with apoptosis [15] and necrosis [16] and were different between nasopharyngeal carcinoma (NPC) cell lines [17, 18]. These applications emphasize the importance of determining the spatially resolved attenuation coefficient in heterogeneous scattering biological tissue.

Determining attenuation coefficient from OCT data is most commonly done by fitting an exponential curve through OCT depth profiles. This approach requires tissue with a relatively uniform attenuation coefficient over a certain depth. Depending on the amount of noise, a lot of data needs to be averaged before a reliable exponential fit is obtained. Due to averaging the data, the attenuation coefficient can only be determined globally, or spatially, albeit with a very low resolution. It also requires pre-segmented data to ensure averaging over areas with a relatively uniform attenuation coefficient. Alternatively, a different method based on a reference layer in the data [19] may be used. It results in a high lateral resolution for the estimated attenuation coefficients [14], but requires the presence of such a reference layer and a robust segmentation thereof [20].

In this paper, we present an approach to determine the depth-resolved attenuation coefficient from OCT data and experimentally verify the method on multi-layered scattering phantoms. It is based on a single-scattering model and exploits the common property in OCT imaging that the majority of the light is attenuated within the imaging depth range. The resulting attenuation coefficients are estimated locally; every pixel in the OCT data set is converted into a corresponding pixel in the attenuation coefficient data set. No segmentation is required to determine these attenuation coefficients. We present numerical simulations to characterize the reconstruction algorithm's properties. The method is validated on uniform phantoms and phantoms comprising of multiple layers with different attenuation coefficients. Finally, an in-vivo example of the resulting attenuation coefficient images is shown to demonstrate the ability to

spatially resolve the attenuation coefficient at pixel resolution. Additionally, it illustrates the method's robustness to shadowing and other common OCT imaging artifacts.

2. Attenuation coefficient estimation

The most commonly employed way to determine attenuation coefficients from OCT is based on fitting an exponential curve to the OCT signal. This method is described in more detail below. Subsequently, a different method is introduced for local attenuation coefficient estimation that does not require a thick and uniform layer or the presence of a reference layer.

2.1. Exponential curve fit

The detected OCT signal power $I(z)$ that is proportional to the reflected intensity from the sample and results from scattering at a certain depth z in a homogeneous medium, may be described by [21]

$$I(z) \propto e^{-2\mu z}. \quad (2)$$

Here, the factor 2 is due to the light propagating through the tissue twice. The attenuation coefficient may now be estimated by differentiating the logarithm of the OCT signal:

$$\hat{\mu} = -\frac{1}{2} \frac{d \log(I(z))}{dz}, \quad (3)$$

where $\hat{\mu}$ is the estimated value for the attenuation coefficient. Because of the derivative in the equation, this local estimation of the attenuation coefficient is very sensitive to the presence of speckle noise in the OCT data. Therefore, this method is replaced by fitting an exponential function to the data over a certain depth range, e.g. until the signal is attenuated to a factor of e^{-1} [6] or until the integrated backscattered signal reaches a predefined threshold [11], to obtain an estimate of the attenuation coefficient [22]. We propose the product of μ and the fitting range d as a quality estimator for the fit. The aforementioned attenuation factor of e^{-1} then corresponds to $\mu \cdot d = \frac{1}{2}$. A smaller product indicates a small range relative to the attenuation length over which the slope is fitted, leading to a less reliable result. A larger product indicates a large range relative to the attenuation length over which the slope is fitted, leading to a more reliable result.

Because the exponential fit is done over a certain depth range, the image should only contain a single tissue type, or the region of interest has to be selected prior to fitting the exponential curve. Refinements of this model, for example to include the axial point spread function (PSF) [23], have been proposed, but these do not solve the mentioned inherent limitations of the curve fitting approach.

2.2. Depth-resolved method

The main problem with the curve fitting method of section 2.1 is that it requires a considerable amount of data points along a depth profile (A-line) to robustly and accurately estimate the attenuation coefficient from the exponentially decaying slope. In this section, we describe a method, originally introduced for ultrasound imaging, that builds on two assumptions: almost all light is attenuated within the recorded imaging depth range and the backscattered light that is reflected towards the OCT system's photo detector is a fixed fraction of the attenuated light. These assumptions enable estimation of attenuation coefficients for every pixel in the data set, without the need for a reference layer. Multiple scattered light is not taken into account.

2.2.1. Model of light-tissue interaction measurements

The differential equation for the attenuation of a coherent light beam, according to Lambert-Beer's law, is given by

$$dL(z) = -\mu(z)L(z) dz, \quad (4)$$

where $\mu(z)$ (expressed in mm^{-1} , z expressed in mm) is now the depth-dependent attenuation coefficient. This equation provides a linear relationship between the amount of attenuated irradiance and the irradiance of the incident light beam ($L(z)$). The factor that relates the attenuated and the incident power is the attenuation coefficient. With a boundary condition of $L(0) = L_0$, where L_0 is the irradiance of the incident light beam (expressed in W m^{-2}) at depth $z = 0$, solving this equation yields

$$L(z) = L_0 e^{-\int_0^z \mu(u) du}. \quad (5)$$

A constant attenuation coefficient reduces this formula to Eq. (1). The equation with depth-dependent attenuation coefficients can only be solved if L_0 and all attenuation coefficients are known.

Attenuation results from both scattering and absorption. Assuming a fixed fraction α of the attenuated light is back scattered, the irradiance density (i.e., irradiance per unit depth, expressed in $\text{W m}^{-2} \text{mm}^{-1}$) of the back scattered light at depth z is given by

$$B(z) = -\alpha \frac{dL}{dz} = \alpha \mu(z)L(z) = \alpha \mu(z)L_0 e^{-\int_0^z \mu(u) du}. \quad (6)$$

The signal that is actually detected by the OCT device is not equal to $B(z)$. Instead, it is first attenuated on its way from the scattering site to the detector according to

$$S(z) = B(z) e^{-\int_0^z \mu(u) du} = \alpha \mu(z)L_0 e^{-2\int_0^z \mu(u) du}, \quad (7)$$

where $S(z)$ is expressed in $\text{W m}^{-2} \text{mm}^{-1}$. Finally, the back scattered irradiance is detected and converted into a digital signal

$$I(z) = \beta S(z) = \alpha \beta \mu(z)L_0 e^{-2\int_0^z \mu(u) du}, \quad (8)$$

where $I(z)$ is the resulting OCT signal and β is a conversion factor that accounts for the digitization of the signal and the integration of the signal corresponding to the size of the detector and the axial sampling density.

2.2.2. Estimating the attenuation coefficient

The indefinite integral of $I(z)$ is now given by

$$\int I(z) dz = \alpha \beta L_0 \int \mu(z) e^{-2\int_0^z \mu(u) du} dz \quad (9)$$

$$= -\frac{\alpha \beta L_0}{2} e^{-2\int_0^z \mu(u) du} + C \quad (10)$$

$$= -\frac{I(z)}{2\mu(z)} + C \quad (11)$$

With the boundary condition $I(\infty) = 0$, the following definite integral may be defined:

$$\int_z^\infty I(u) du = -\frac{I(u)}{2\mu(u)} + C \Big|_z^\infty = \frac{I(z)}{2\mu(z)} \quad (12)$$

Solving this equation for $\mu(z)$ and taking the limited depth range D of OCT systems into account yields

$$\mu(z) = \frac{I(z)}{2 \int_z^\infty I(u) du} \approx \frac{I(z)}{2 \int_z^D I(u) du} \quad (13)$$

A similar result was derived earlier for ultrasound signal compensation by Hughes and Duck [24], although the above derivation is somewhat simpler. In addition to other domain-specific constants, Hughes and Duck used a different, more complex model to relate attenuation and backscattering. However, those model parameters need to be specified in advance and were not derived from the data. Our model contains no such user-specified parameters.

2.2.3. Discretization

The OCT signal $I(z)$ was defined on a continuous domain in Eq. (8), but only discretized measurements are available. These measurements $I[i]$ are given by the integrated signal over a small distance, defined by the pixel size Δ and commonly related to the coherence length of the light source. Let u denote the lower and v the upper boundary of a pixel, such that $u = i\Delta$, $v = u + \Delta$ and $u \leq z < v$. Then, the available measurements are related to the OCT signal by $I[i] = \int_u^v I(z) dz$. Approximating $I(z)$ by a constant value $I(u)$ over a pixel gives $I[i] = \Delta I(u)$.

The attenuation coefficient corresponding to a certain pixel is defined by the average attenuation over the pixel size. Based on Eq. (13), this is given by

$$\mu[i] = \frac{1}{\Delta} \int_u^v \mu(z) dz = \frac{1}{\Delta} \int_u^v \frac{I(y)}{2 \int_y^\infty I(z) dz} dy. \quad (14)$$

Again assuming that $I(z)$ is constant over a pixel results in

$$\mu[i] = \frac{1}{2\Delta} \int_u^v \frac{I(u)}{\int_y^\infty I(u) dz + \int_v^\infty I(z) dz} dy \quad (15)$$

$$= \frac{1}{2\Delta} \int_u^v \frac{I(u)}{(v-y)I(u) + A} dy, \quad (16)$$

where $A = \int_v^\infty I(z) dz = \sum_{i+1}^\infty I[i]$. Using $\int \frac{I(u)}{(v-y)I(u) + A} dy = -\log(A + (v-y)I(u))$, the integral can be solved:

$$\mu[i] = \frac{1}{2\Delta} \log \left(1 + \frac{\Delta I(u)}{A} \right) = \frac{1}{2\Delta} \log \left(1 + \frac{I[i]}{\sum_{i+1}^\infty I[i]} \right). \quad (17)$$

This equation was used in all experiments in this paper. A first-order linearization of $\log(1+x)$ around $x=0$ may be employed to further simplify the expression for the attenuation coefficient:

$$\mu[i] \approx \frac{I[i]}{2\Delta \sum_{i+1}^\infty I[i]}. \quad (18)$$

3. Results

In this section, we first present numerical simulations to explain some of the properties of this method and how violating the model assumptions affect the reconstructed attenuation coefficients. Then, in section 3.2, phantom experiments on both uniform and layered phantoms are presented to assess the accuracy of the attenuation coefficient estimation method. Finally, the method is applied to in-vivo measurements of the retina in section 3.3.

3.1. Numerical simulations

First, numerical simulations were performed by the same single scattering model that was used to derive the attenuation coefficient estimation. OCT depth profiles were calculated based on Eq. (8), with arbitrary values for α , β and L_0 ($\alpha = 0.5$, $\beta = 2$, $L_0 = 1$). The axial resolution was set to $4\ \mu\text{m}$ and each depth profile contained 500 pixels. For the first experiment, the thick simulated tissue, with an attenuation coefficient of $5\ \text{mm}^{-1}$ was placed at $200\ \mu\text{m}$ from the zero delay line. The simulated OCT signal is shown in Fig. 1(a) (solid blue line). The attenuation coefficients along the depth profile were calculated with the procedure described in section 2.2 and are shown in Fig. 1(b) (solid blue line). The attenuation coefficient at a distance of around $200\ \mu\text{m}$ was estimated to be $5\ \text{mm}^{-1}$, very accurately matching the real simulated attenuation coefficient. Towards the end of the depth profile, however, the estimated attenuation coefficient becomes much larger. This is due to violation of the assumption that all light is attenuated within the imaging depth range. In our simulation not all light has been attenuated at a depth of $2\ \text{mm}$. This leads to an overestimation of the attenuation coefficient near the end of the depth profile.

Displacing the tissue backwards in steps of $400\ \mu\text{m}$ shows that the estimated attenuation coefficients near the front of the tissue are unaffected by its position (see the dashed lines in Fig. 1(b)). This illustrates that the model estimates the local power of the incident light beam from OCT signals from larger depths only, as expressed by the range of integration in Eq. (13).

Examples of different attenuation coefficients ($1\ \text{mm}^{-1}$, $2\ \text{mm}^{-1}$, $5\ \text{mm}^{-1}$ and $10\ \text{mm}^{-1}$) are shown in Fig. 2 (solid lines). Increasing errors are observed near the end of the imaging depth range and for small attenuation coefficients. For these attenuation coefficients, a significant amount of light is not attenuated within the imaging depth range, thereby violating a key assumption of the model that all light is attenuated within the imaging depth range.

To evaluate the performance of the attenuation coefficient estimation on layered structures, a simulation was run on an assembly of tissues with different attenuation coefficients. Each layer was $360\ \mu\text{m}$ thick, and had an attenuation coefficient of $0.5\ \text{mm}^{-1}$, $1\ \text{mm}^{-1}$, $2\ \text{mm}^{-1}$, $5\ \text{mm}^{-1}$ and $10\ \text{mm}^{-1}$, respectively. The simulated OCT depth profile and the reconstructed attenuation coefficients are shown in Fig. 2 (dashed line). The median estimated attenuation coefficients for each layer were $0.502\ \text{mm}^{-1}$, $1.00\ \text{mm}^{-1}$, $2.01\ \text{mm}^{-1}$, $5.02\ \text{mm}^{-1}$ and $10.3\ \text{mm}^{-1}$, respectively. Similar to the single layer examples, the errors increase towards the end of the imaging

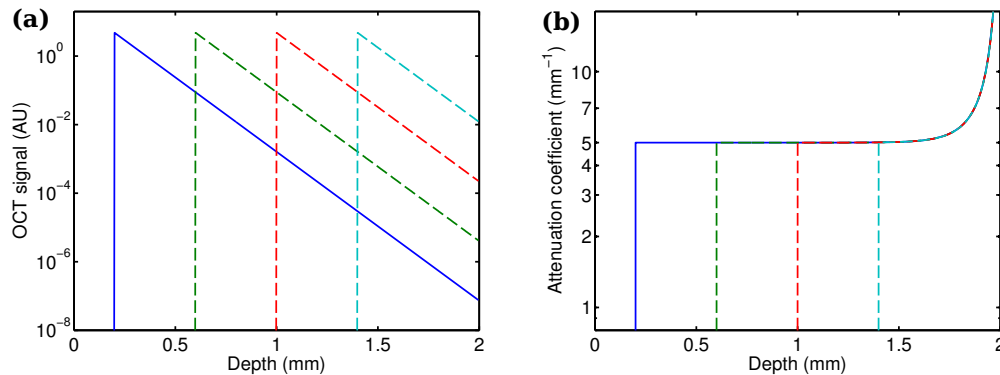


Fig. 1. Simulated thick phantom, with its front surface moved back in steps of $400\ \mu\text{m}$. (a) The simulated OCT signal shows a shifted response. (b) The accuracy of the attenuation coefficients that were estimated by Eq. (17) is not affected by moving the object in axial direction.

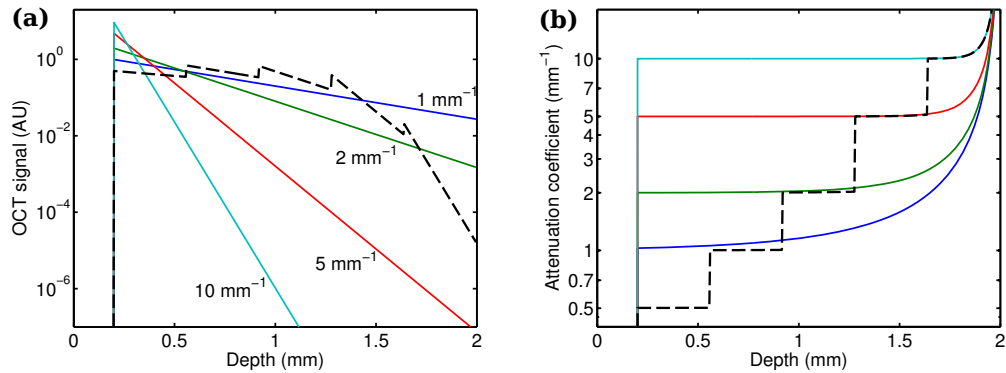


Fig. 2. (a) Simulated OCT signals and (b) estimated attenuation coefficients (Eq. (17)) for uniform and layered phantoms with various attenuation coefficients. *Solid lines*: Simulated thick phantoms, with attenuation coefficients of 1 mm^{-1} , 2 mm^{-1} , 5 mm^{-1} and 10 mm^{-1} . Different attenuation coefficients result in different slopes in the OCT signal. The proposed method is capable of depth-resolved estimation of the attenuation coefficient from the OCT signal with high accuracy. *Dashed line*: Simulated 5-layer phantom with an individual layer thickness of $360 \mu\text{m}$ and attenuation coefficients of 0.5 mm^{-1} , 1 mm^{-1} , 2 mm^{-1} , 5 mm^{-1} and 10 mm^{-1} . The proposed method can accurately estimated the attenuation coefficient of the various layers.

depth range, but even the deepest layer shows an error of just a few percent.

3.2. Phantom experiments

Perfect exponential decay of a noiseless OCT signal is a rather unrealistic model for real data from heterogeneous tissue. Therefore, we developed phantoms with known and controlled properties to verify the attenuation coefficient estimation method experimentally.

3.2.1. Manufacturing of phantoms

Manufacturing of the phantoms used for our experiments was based on a previously described protocol [25]. A mixture of 1 w% TiO_2 particles in silicone was prepared by first mixing TiO_2 powder ($\geq 99\%$, part number 14021, Sigma-Aldrich) with the curing agent part of Sylgard 184 (Dow Corning). This low viscosity suspension was then sonicated at 137 kHz for 90 minutes in an ultrasonic bath. After mixing this suspension with the elastomer part of Sylgard 184 (mixing ratio 1:10), it was degassed at 8 mbar in a vacuum chamber. To produce lower concentrations of TiO_2 , the suspension was diluted with a transparent curing agent - silicone elastomer (1:10) mixture to the desired concentrations. The refractive index of the transparent suspension was measured to be 1.44. Phantoms with uniform scattering properties were produced from the resulting mixtures.

Layered phantoms were mounted on a substrate, which was produced by curing approximately 20 g of silicone - TiO_2 mixture inside a Petri dish. The layers were produced by sandwiching a drop of silicone - TiO_2 mixture between two glass plates separated by spacers with a thickness of $170 \mu\text{m}$ to control the thickness. After curing, the layers were retrieved from the glass plates, mounted onto each other and cut into a 1 cm^2 square. Undesired air between the layers was removed by decompressing the layered structure in a vacuum chamber.

3.2.2. Acquisition and preprocessing of data

The OCT measurement on all phantoms were performed with an experimental optical frequency domain imaging system [26]. The laser source (Axsun Technologies Inc., MA, USA) swept from 1258 nm to 1366 nm at 50 kHz, producing approximately 29 mW of output power. With a depth resolution in air of 10 μm , the axial resolution in the medium was 7 μm . The light from the source was split by a 99/1 fiber coupler and 1% of the light was used to generate an optical trigger pulse. The large portion (99%) was further split by a 90/10 fiber coupler and subsequently directed into the sample arm (90%) and the reference arm (10%) by two fiber-optic circulators. The same circulators were used to redirect the backscattered light from both arms into a 50/50 fiber coupler for balanced detection with a balanced amplified photodetector (PDB430C, 800 nm to 1700 nm, 350 MHz, Thorlabs, Newton, NJ, USA). Then, the measured signal was digitized to 12 bits. An achromatic lens with 45 mm focal length was used to focus the light with a beam diameter of 3.4 mm and collect the backscattered photons. The Rayleigh length of the optical setup was 292 μm (in air) and the diameter of the focal spot was approximately 22 μm . B-scans were produced by a laterally scanning galvo mirror system.

Each phantom was mounted slightly tilted with respect to the OCT beam to minimize surface reflections back into the detection system. The phantom was perpendicular to the OCT beam in the fast scanning direction, but due to the tilt the depth of the phantom in the image differed between B-scans. Of each phantom, 205 B-scans were acquired that composed a volume scan.

After acquisition, each measured interference spectrum was discrete Fourier-transformed to obtain a complex depth profile or A-line. Then, the average of a large number of A-lines was subtracted from every A-line to remove fixed pattern noise. Subsequently, the power magnitude of each A-line ($U(z)$) was calculated by squaring the complex depth profile. The following corrections were made to compensate for the noise floor and the depth-dependent signal decay: First, a background image was acquired by blocking the sample arm and a large number of acquired A-lines were averaged. The resulting noise floor signal $N(z)$ was subtracted from all phantom measurements. The signal decay $S(z)$ was modeled by a Gaussian ($S(z) = \exp(-z^2/\sigma^2)$). Its width σ was determined from sensitivity measurements, which showed 3 dB loss at 4.7 mm (in air). Each A-line of the phantom measurements was divided by this signal decay factor. For all scans acquired from the phantoms, the corrected data $I(z)$ was then calculated from the data $U(z)$ by

$$I(z) = \frac{U(z) - N(z)}{S(z)}. \quad (19)$$

The resulting, corrected images of the phantoms were transformed to attenuation coefficient

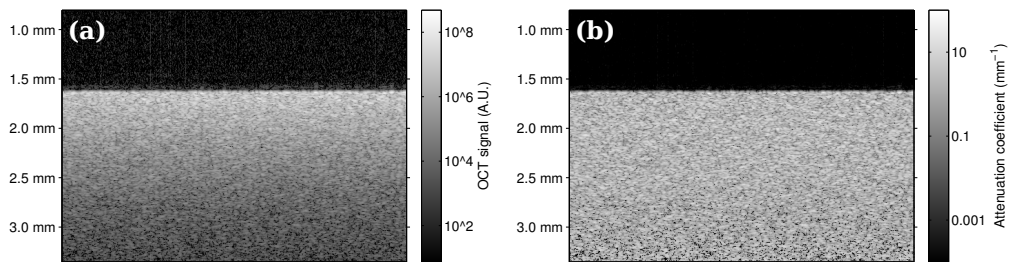


Fig. 3. (a) OCT image data from uniform phantoms. (b) Corresponding attenuation coefficient image. The proposed method transforms every pixel in the OCT image from a value expressed in arbitrary units into an attenuation coefficient with a physical unit of measurement.

Table 1. Attenuation coefficients estimated by the OCT slope method (Eq. (3)) from the uniform phantoms (205 B-scans per phantom, fitted over 0.5 mm) for different TiO₂ weight concentrations. The large amount of data available for the fitting procedure resulted in a standard error smaller than 0.02 mm⁻¹ for all phantoms.

TiO ₂ conc. (w%)	0	0.01	0.025	0.05	0.1	0.25	0.5	1
OCT slope (mm ⁻¹)	0.04	0.28	0.20	0.59	0.98	2.8	4.9	7.6

images (see Fig. 3). Both the OCT images and the attenuation coefficient images were then averaged in the scanning direction. This resulted in a single A-line for each B-scan of the OCT data and a single A-line for each attenuation coefficient image, both with reduced noise.

3.2.3. Uniform phantoms

Eight thick phantoms were created with 0 w%, 0.01 w%, 0.025 w%, 0.05 w%, 0.1 w%, 0.25 w%, 0.5 w% and 1 w% of TiO₂. Each phantom was measured as described above and for each phantom all 205 B-scans were recorded. To evaluate the reference method and to verify that the attenuation coefficient of our phantoms depended linearly on the particle concentration, the attenuation coefficient was estimated for each phantom by simultaneously fitting the OCT signal of all 205 B-scans with a single exponential decay, the slope of the curve of the OCT signal that was derived from each B-scan. In this fitting procedure, the slope was fitted over 0.5 mm for all 205 averaged B-scans.

The estimated attenuation coefficients are shown in Table 1 and in Fig. 4. Theory predicts a linear relationship between particle concentration and attenuation coefficient for relatively small weight concentrations, which was indeed observed in the data (slope of 9.8 mm⁻¹ w%⁻¹, $R^2 = 0.97$, $p < 10^{-5}$). The large amount of averaging in this case provided accurate attenuation coefficients even when the quality factor $\mu \cdot d$ is much smaller than $\frac{1}{2}$ (e.g., the quality factor is 0.05 for a concentration of 0.025 w%). Using the full volumetric dataset, an excellent linear relation between particle concentration and attenuation coefficient as determined by fitting the

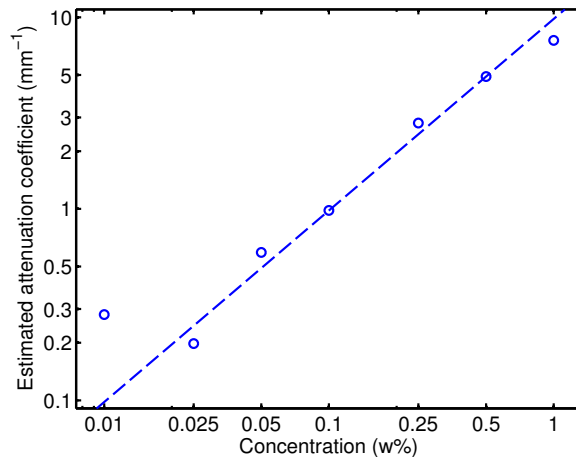


Fig. 4. Attenuation coefficients determined by fitting an exponential curve to the OCT data (205 B-scans per phantom; the curve was fitted over 0.5 mm). The dashed line is a robust fit (with bisquare weights) of the linear model $\log(y_i) = \log(bx_i) + \varepsilon_i$.

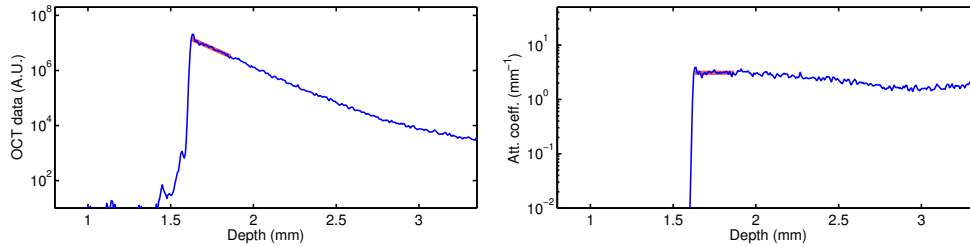


Fig. 5. Depth profiles (blue lines) and fits (thick red lines) for OCT data (left) and attenuation coefficient images (right) for a uniform phantom with 0.25 w% TiO_2 . The fits were based on the data corresponding to the thick red lines (depth range of 0.25 mm).

slope of the decay of the OCT signal was found. Only the estimated attenuation coefficient for the 0.01 w% does not comply with this linear relationship. In this case, the expected attenuation over the fitting depth is very small (about 1 % for $\mu = 0.1 \text{ mm}^{-1}$).

To compare the attenuation coefficients as determined by fitting the slope of the signal decay and by our proposed method, single B-scans were analyzed. The attenuation coefficient was first estimated by fitting the slope of the curve of the OCT signal. Then, the average attenuation coefficient from the proposed method was calculated over the same depth that was used for the fitting procedure. An example of the fits is shown in Fig. 5, corresponding to the data of the phantom in Fig. 3.

The attenuation coefficients for each phantom resulting from both methods are listed in Table 2. Figure 6 shows the same data, including the 95% confidence interval of the fit for each estimated value. Also indicated are the fitted lines for the model $y = a + bx$, where x is the concentration and y is the estimated attenuation coefficient. The fitted values for a and b were 1.2 mm^{-1} and $7.6 \text{ mm}^{-1} \text{ w\%}^{-1}$, respectively, for the OCT slope method and 0.9 mm^{-1} and $8.8 \text{ mm}^{-1} \text{ w\%}^{-1}$ for the proposed method. The factors relating the concentration to the attenuation coefficient are consistent for both methods. For concentrations above approximately 0.1 w%, the behavior is linear for both methods. For concentrations below 0.1 w%, where the quality factor is significantly lower than 0.5, the relation is no longer proportional and the variance of the estimates based on the slope increase considerably.

Table 2. Attenuation coefficients (standard error) estimated by the OCT slope method (Eq. (3)) and the proposed method (Eq. (17)) from the uniform phantoms (fitted over 0.25 mm) for different TiO_2 weight concentrations.

TiO_2 conc. (w%)	OCT slope (mm^{-1})	μ (mm^{-1})
0	1.1 (0.8)	0.85 (0.12)
0.01	1.5 (0.3)	0.83 (0.04)
0.025	1.3 (0.16)	1.1 (0.02)
0.05	1.7 (0.15)	1.4 (0.02)
0.1	1.6 (0.12)	1.8 (0.03)
0.25	3.1 (0.10)	3.1 (0.04)
0.5	5.3 (0.13)	5.2 (0.07)
1	8.8 (0.17)	7.8 (0.2)

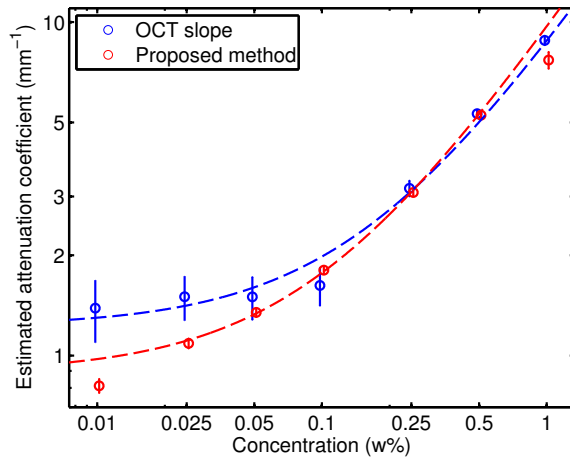


Fig. 6. Attenuation coefficients determined by fitting an exponential curve to the OCT data (blue) and by the proposed method (red), over a depth of 0.25 mm. The circles denote the measurements and the vertical lines indicate the 95% confidence interval. The dashed lines are robust fits (with bisquare weights) of the model $\log(y_i) = \log(a + bx_i) + \varepsilon_i$.

3.2.4. Multi-layer phantoms

To better match the morphology of the retina, a layered phantom was created. The phantom consisted of five thin layers, mounted on a thick substrate. The layers were created from solutions containing 0.5 w%, 0.05 w%, 0.25 w%, 0.025 w% and 0.1 w% of TiO_2 . Every layer was about 0.17 mm thick and the substrate contained 0.25 w% TiO_2 . Averaged A-line profiles of both OCT measurements and attenuation coefficient images are shown in Fig. 7 (blue lines).

The OCT signal was first analyzed by curve fitting each layer. The points corresponding to the thick red solid line in Fig. 7 (left) were used for the fit. The estimated slopes are listed in Table 3. Because of the large number of A-lines that were averaged and the relatively large number of pixels per layer (approximately 25), the curve fitting technique results in negative slopes for all layers. However, the magnitude of the slopes are sometimes inconsistent: The third and fourth layer show similar slopes while their concentration differ by a factor of 10.

The attenuation coefficients were also calculated by our model-based method. The average value for every layer was calculated from the data corresponding to the thick red solid lines

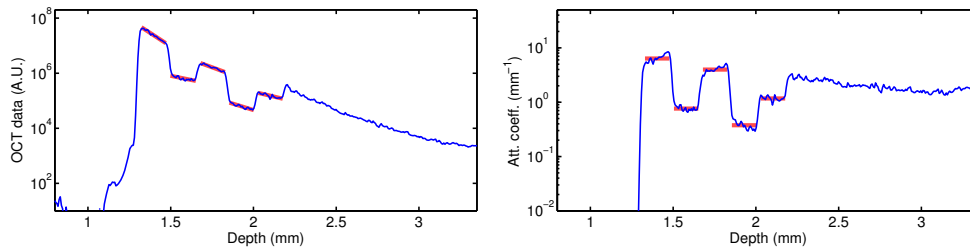


Fig. 7. Layered phantom depth profiles of the OCT signal (left) and the per-pixel attenuation coefficients estimated by the proposed method (right). The fits were based on the data corresponding to the thick red lines (depth range of 0.15 mm per layer).

Table 3. Estimated attenuation coefficients from the layered phantom.

Layer	TiO ₂ conc. (w%)	OCT slope (mm ⁻¹)	μ (mm ⁻¹)
1	0.5	4.5 (0.12)	6.4 (0.3)
2	0.05	1.4 (0.3)	0.76 (0.02)
3	0.25	2.6 (0.15)	4.0 (0.1)
4	0.025	2.1 (0.2)	0.38 (0.02)
5	0.1	1.6 (0.2)	1.17 (0.03)

in Fig. 7 (right). The proposed method does not require the fit of a curve, which is inherently sensitive to noise in the data. Instead, the local signal is compared to the integral of the signal from deeper layers and therefore the results are stable even when only a few points are included, such as in the case of thin layers.

The results of both methods are also illustrated by Fig. 8, which shows for each layer the estimated attenuation coefficients including the 95% confidence interval. Again, the model $y = a + bx$, where x is the concentration and y is the estimated attenuation coefficient, was fitted to the data. The estimated values for a and b were 1.4 mm^{-1} and $5.3 \text{ mm}^{-1} \text{ w\%}^{-1}$, respectively, for the OCT slope method and 0.03 mm^{-1} and $13.8 \text{ mm}^{-1} \text{ w\%}^{-1}$ for the proposed method. Due to the small fitting range of 0.15 mm, the quality factor $\mu \cdot d$ is above 0.5 for the first layer only; for all other layers, the quality factor $\mu \cdot d$ is smaller than 0.5 and the OCT slope method is expected to produce less reliable results. In contrast, the proposed method shows excellent linear correlation between the estimated attenuation coefficient and the TiO₂ concentrations of the layers.

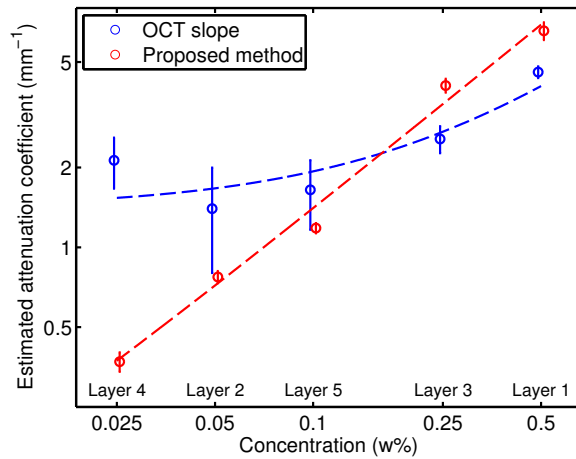


Fig. 8. Estimated attenuation coefficients for the layered phantom by exponential fits (in blue) and the presented method (in red), over a depth of 0.15 mm for each layer. The circles denote the measurements and the vertical lines indicate the 95% confidence interval. The dashed lines are robust fits (with bisquare weights) of the model $\log(y_i) = \log(a + bx_i) + \varepsilon_i$.

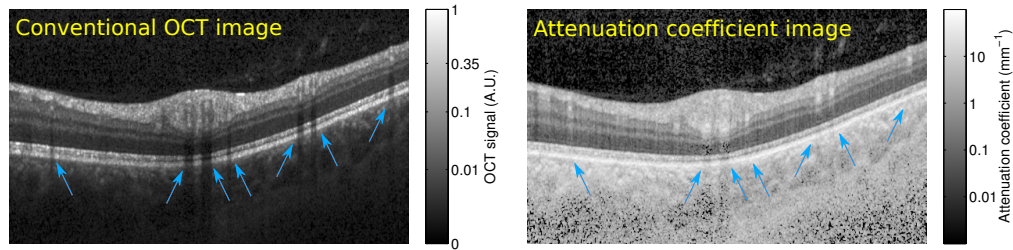


Fig. 9. In-vivo retinal scan of a normal subject. The OCT scan (*left*) was transformed according to the manufacturer's recommendations for display purposes only ($\sqrt[4]{}$). Areas with OCT shadowing due to blood vessels are indicated by blue arrows. The attenuation coefficient (*right*) of deeper layers at these locations is largely unaffected.

3.3. In-vivo example

A volumetric, peripapillary scan was acquired from a normal eye with a commercially available Spectralis (Heidelberg Engineering, Germany) OCT system. This scan came from an ongoing study on glaucoma imaging at the Rotterdam Eye Hospital. All procedures adhered to the tenets set forth in the Declaration of Helsinki.

The Spectralis OCT system operates at 850 nm, has a spectrum analyzer and employs eye tracking to stabilize eye motion during acquisition. Eye tracking also allowed averaging of multiple B-scans, acquired at the same location, to increase signal to noise ratio. Per volume, 193 B-scans were acquired; each B-scan was the average of 5 original B-scans. Every B-scan consisted of 512 A-lines, containing 496 pixels.

Figure 9 (left) shows an example retinal B-scan. It clearly shows shadowing due to blood vessels, mainly affecting the signal in deeper layers such as the photoreceptors and the RPE. In the presence of floaters, similar shadowing effects affect the signal magnitude of all layers in specific parts of the scan.

Figure 9 (right) shows the corresponding attenuation coefficient image. The shadowing artifacts are largely gone and every pixel is now associated with a meaningful unit of measurement (see color bar), rather than with arbitrary units. In the choroid and especially in the sclera, the signal is very noisy, due to the small amount of light that reaches these deeper parts of the eye.

4. Discussion

We presented a method for depth-resolved reconstruction of attenuation coefficients from OCT data that is based on a single-scattering model. This resulting approach is similar to a method for attenuation compensation in ultrasound [24]. While attenuation compensation has been applied to OCT data before in the context of contrast enhancement [27], our more ambitious goal is to employ the attenuation coefficient estimation for quantitative analysis. Our results from the first presented validation experiments are very promising in this respect: The phantom experiments show that the presented method is capable of accurately estimating the attenuation coefficients in both uniform and layered, heterogeneous phantoms, except when the key assumption of the model that all light is attenuated within the imaging depth range is violated, such as for our uniform phantoms with low attenuation coefficients. In layered phantoms, a remarkably strong linear correlation was found between estimated attenuation coefficients and the concentration of scattering particles, even for low attenuation coefficients and small concentrations, because the scattering substrate preserved the key assumption of the model. In contrast, the OCT slope method produces unreliable results when the product of attenuation coefficient and fitting depth is smaller than 0.5.

Numerical experiments illustrated several properties of the method: The attenuation coefficient estimation procedure does not depend on the position of the tissue within the imaging depth range, it produces the correct attenuation coefficient except towards the end of the imaging depth if the key assumption is violated and it works on layered objects with different attenuation coefficients. Then, experiments were performed on uniform and layered phantoms and attenuation coefficients were estimated by the proposed method and the slope method. We showed comparable results for both methods on the uniform samples. On the layered phantoms, the slope estimation proved to be unreliable due to the low quality factor (smaller than 0.5 for most layers). The proposed method produced consistent results for all layers. Processing of in-vivo retinal images indicated that the estimated attenuation coefficients do not suffer from common artifacts. Deeper layers were largely continuous, without showing gaps due to shadows of blood vessels.

A straightforward single-scattering model of the propagation of light in a medium was used. The axial PSF was not taken into account in either attenuation coefficient estimation method. Including the axial PSF in the model that describes the OCT signal of a uniform medium results in [22,23]

$$I(z) \propto \frac{e^{-2\mu z}}{\left(\frac{z-z_0}{2z_R}\right)^2 + 1}. \quad (20)$$

Here, z_0 is the depth-location of the point of focus, and z_R is the Rayleigh length in the medium. The OCT slope method estimates the slope of the logarithm of the signal and is affected by the bias. By substituting Eq. (20) in Eq. (3), the magnitude of this effect can be estimated:

$$\hat{\mu} = -\frac{1}{2} \frac{d \log(I(z))}{dz} = \mu + \frac{z - z_0}{(z - z_0)^2 + 4z_R^2}. \quad (21)$$

The second term of this equation represents the bias due to the axial PSF. At $z = z_0 \pm 2z_R$, this bias reaches its maximum of $\pm 1/(4z_R) = \pm 0.59 \text{ mm}^{-1}$. The bias depends on z , z_0 and z_R , but not on the attenuation coefficient and its contribution is therefore significant for low attenuation coefficients only. In our experiments, the point of focus was above the phantom and the introduced bias is therefore positive. For low attenuation coefficients, the estimated value based on the slope of the OCT signal is thus larger than the real attenuation coefficient. This explains the deviation of the estimated attenuation coefficients from a straight line in Fig. 6 for low concentrations of TiO_2 .

An assumption of the proposed method is that most of the incident light is attenuated within the imaging depth range. In most biological samples, this is indeed the case, although it does not hold when most of the sample is transparent, such as in the anterior segment of the eye. In the thick phantoms with low concentrations of TiO_2 , this assumption does not hold either, which introduces an error in the low attenuation coefficient measurements. In the layered phantom, most of the light is attenuated within the depth range, and in those cases the method can indeed reliably estimate even small attenuation coefficients.

For many applications, with relatively low scattering coefficients (i.e., smaller than approximately 10 mm^{-1}), a single scattering model describes the scattering effects in OCT imaging with sufficient accuracy [22, 28]. However, multiple scattering has been studied in the past in the context of OCT [29] and may be incorporated in the proposed model to broaden its validity to higher scattering coefficients.

The presented method provides a way to estimate attenuation coefficients at a much higher resolution than by existing approaches, by modeling the OCT signal based on single scattering of light in tissue. It does not require segmentation prior to attenuation coefficient estimation. It therefore enables new quantitative and functional analyses of heterogeneous or compound

structures in a wide range of OCT applications, providing novel tools for diagnosis and monitoring of various diseases.

Acknowledgments

This research was (partially) funded by Stichting Combined Ophthalmic Research Rotterdam and the Netherlands Organization for Scientific Research (NWO) through a ZonMW TOP grant (40-00812-98-12061) and VICI grant (918.10.628, JFdB).